6.1. Introduction

Frictional losses are a major source of concern in all mechanical systems. Such losses must be strictly limited in order to extend their service life and conserve energy. Controlling friction at the nanoscale is an important field of research today. Because of their great flexibility and mechanical strength, several 2D materials such as layered metal hydroxides, metal chalcogenides, graphitic carbon nitride, etc. have been preferred as friction and wear-diminishing agents in base lubes.[1-3]

Metal-organic frameworks (MOFs) are a novel class of crystalline materials that comprises 3D/2D networks generated through the interaction of metal ions with the bridging organic ligand (s).[4-6] MOFs have found widespread use in catalysis, gas sorption, sensing, electrochemical applications, gas separation, energy storage, and energy conversion.[7-10] Recently, MOFs have brought consideration in tribology due to their appealing features for instance variable porosity, broad surface area, and long thermal as well as chemical stability [11]. For example, 3D-structured zeolitic imidazolate frameworks (ZIF), and nanocrystalline ZIF-8 improved the antiwear performance and load-carrying abilities of the PEG200 base lube by 31.35% and 7.60%, respectively whereas microcrystalline ZIF-8 improved these properties by 30.76% and 17.25%, respectively.[12] The poor dispersibility of 3D MOF materials in base oil makes friction reduction to a limited extent.[13] Gao et al. have demonstrated that the mechanical and tribological performance of 2D Ni-Fe MOF-assisted poly(vinyl alcohol) hydrogels was much better due to enhanced dispersibility.[14] Ultrathin Zn-BDC and mesoporous Cu-BTC-MOFs have also been reported to show good lubricating behavior.[13,15] We have also found

enhanced tribological activity of 2D ultrathin Mn-BDC MOF (BDC=1,4-benzene dicarboxylic acid) over bulk 3D MOF in our laboratory.[16] Thus, the lamellar structure of 2D MOFs is favorable in upgrading dispersibility in the base oil, resulting in improved mechanical and tribological performance. Accordingly, the present investigation was intended for the synthesis of Ni-Mn based bimetallic-organic framework (NMF).

Metal vanadates, these days have attracted a lot of attention from researchers to produce effective photocatalysts for water oxidation and photoelectrochemical activities for water splitting.[17-19] However, the tribological characteristics of metal vanadates, have received little attention. Silver vanadate has been used for lubrication at higher temperatures.[20, 21] Fengzhen et al. have studied the $CeVO_4$ nanoparticles as lubricating additives in liquid paraffin.[22] Though bismuth vanadate ($BiVO_4$) with a significantly positive valence band edge of 2.86 eV and suitable direct bandgap (2.4 eV) has been used as a photocatalyst,[17-19] tribological studies have not yet been conducted. The present scenario fascinated us to explore the lubricating behavior of $BiVO_4$.

Apart from nanoparticles and nanosheets, nanorods have shown aspiring outcomes in tribology. Nanorods of Fe_3O_4, TiO_2, ZnO, Fe_2O_3, CuS, MnO_2, Al_2O_3, and lanthanum borate have been utilized notably for friction reduction.[23-32] Therefore nanorod morphology of $BiVO_4$ was considered for the investigation.

Furthermore, advancement in the lubricating behavior of doped nanomaterials in comparison to undoped ones has been reported by our group such as Ce-doped zirconia, Mg-doped zinc oxide, N-doped zinc oxide, La-doped yttria, and La-doped zinc borate.[33-39] Since we have found encouraging results with nitrogen-doped zinc oxide nanorods, it

appealed us to investigate the tribological behavior of $BiVO_4$ nanorods suitably doped with a metal. Literature reports revealed that molybdenum doping in $BiVO_4$ increases its photocatalytic and electrochemical activities,[17-19] correspondingly it was planned to prepare Mo-doped $BiVO_4$ nanorods foreseeing a good outcome of tribological properties. Additionally, the phenomenal tribological performance of composites made of lamellar nanosheets such as graphene, g-C_3N_4, MoS_2, and vanadium selenide with doped nanomaterials has been established from our laboratory.[33,34,37-39] Consequently, the present investigation includes the synthesis and characterization of $BiVO_4$ (BV) and Mo-doped $BiVO_4$ (MBV) nanorods, 2D Ni/Mn-MOF (NMF) nanosheets, and their composite MBV/NMF, and exploring their applications as potential friction and wear modifiers based on ASTM D4172 and ASTM D5183 test results.

6.2. Experimental Section

6.2.1. Preparation of Nanoadditives

6.2.1.1. *Synthesis of Bismuth Vanadate and Mo-doped Bismuth Vanadate Nanorods*

For the preparation of $BiVO_4$ nanorods (BV), the hydrothermal approach was applied.[40] The solutions of ammonium metavanadate (NH_4VO_3, 7 mmol) in distilled water (80 mL), and bismuth nitrate ($Bi(NO_3)_3{\cdot}5H_2O$, 7mmol) in glacial acetic acid (12 mL) were separately prepared. A yellow precipitate was formed by mixing these two solution. The pH was then roughly adjusted to 9 by adding ammonium hydroxide (NH_4OH) and stirred for 1 h at room temperature. The obtained suspension was then heated for 24 h at 140 °C in a hydrothermal lined with Teflon. After that, the resultant solution was cooled down to ambient temperature, centrifugated, washed with deionized H_2O, dried at around 70-

75 °C for 12 h, and lastly, calcination was carried out for 2 h at 300 °C. For the synthesis of Mo-doped bismuth vanadate(MBV), the same procedure was adopted adding ammonium heptamolybdate [$(NH_4)_6[Mo_7O_{24}.4H_2O$] (0.28 mmol) to the reaction mixture.

6.2.1.2. Preparation of Ni/Mn-MOF Nanosheets

In a 200 mL round bottom flask, distilled water (4 mL), dimethylformamide (64 mL), and ethanol (4 mL) were mixed to form a homogenous solution. It was then mixed with 1.5 mmol of 1,4-benzene dicarboxylic acid (BDC), 0.75 mmol each of $Ni(OAc)_2.4H_2O$, and $Mn(OAc)_2.4H_2O$. The obtained solution was immediately mixed with TEA (triethylamine, 1.6 mL) and stirred for 15 min. The resultant colloidal suspension was continuously sonicated in a nitrogen atmosphere for 4 h at room temperature, followed by centrifugation at 8000 RPM. Finally, the centrifugated product was washed 3-4 times through ethyl alcohol, and then dried under vacuum at ambient temperature.[16]

6.2.1.3. Preparation of nanocomposite MBV/NMF

The NMF nanosheets (300 mg) in ethanol (100 mL) and MBV nanorods (200 mg) in ethanol (80mL), were separately dispersed ultrasonically for 15-20 min at approx 45 °C. Mixed both solutions and ultrasonicated for 1 h at 45 °C to get a homogeneous suspension. The obtained product was filtered, dried, and microwaved (700 W) for 2-3 min. Eventually, a pastel-yellow nanohybrid of MBV with Ni/Mn-MOF was obtained. A schematic representation of the overall synthetic process of hybrid MBV/NMF is demonstrated in Scheme 6.1.

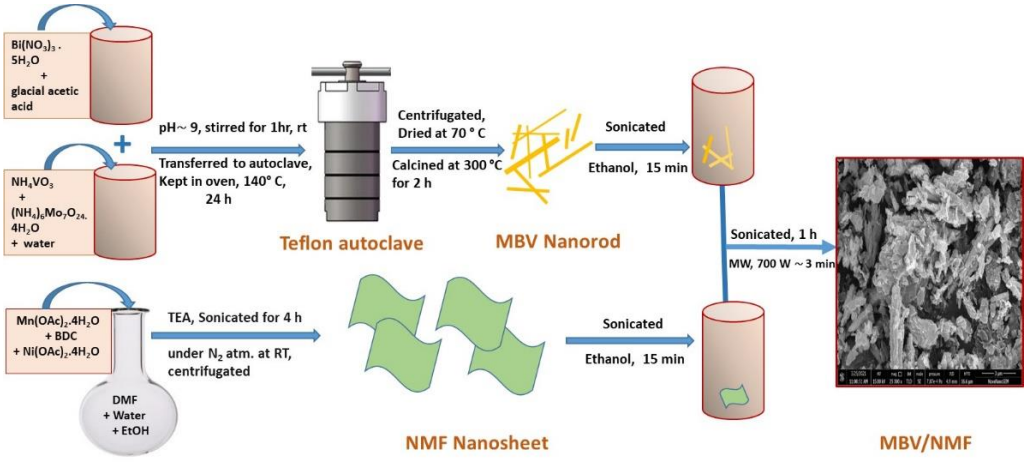

Scheme 6.1. Schematic presentation of preparation of MBV/NMF

6.2.2. Sample preparation

Test samples of different concentrations in the PO, 0.00, 0.10, 0.15, 0.20, and 0.25% w/v were prepared via 1 h sonication at room temperature. The tribological tests were performed at an optimized concentration, i.e., 0.15% w/v in base oil.

6.3. Results and Discussion

6.3.1. Characterization and Morphological study of $BiVO_4$, Mo-doped $BiVO_4$, Ni/Mn-MOF and the hybrid MBV/NMF

The techniques FT-IR, XRD, UV/Visible, SEM/HR-SEM, XPS, and TEM/HR-TEM, were utilized for the characterization of nano additives. Figure 6.1a shows XRD patterns of $BiVO_4$, Mo-doped $BiVO_4$, Ni/Mn-MOF, and MBV/NMF. The formation of BV with a monoclinic single phase was affirmed by the presence of extremely well-precise diffraction peaks corresponding to the JCPDS card number 00-14-0688.[17,18,40] Compared to BV, MBV did not show any significant differences in the characteristic peaks suggesting no considerable effect on the crystal structure of BV after doping with Mo.

However, the characteristic peak of the MBV at 2θ, 29.07 (hkl) plane (121) slightly shifted to a positive angle (0.07) compared to pristine BV showing the successful doping of molybdenum in BV.[17,18] Following CCDC standard card No. 985792, the XRD pattern of Ni/Mn-MOFs has been indexed for diffraction peaks at 8.8, 14.37, 15.45, 17.4, 25.4, 28.7, and 31.4°, which are assigned to the crystal planes (200), (001), (-201), (400), (401), (002), and (-601) respectively.[41,42] This is an indication of monoclinic Ni/Mn-based MOFs without any metal hydroxide/oxide diffraction peaks.[41,42] The heterostructure MBV/NMF did not show any new peaks other than MBV and NMF.

Figure 6.1b. demonstrated the IR spectrum of the synthesized additives. In the spectrum of BV, the symmetric stretching frequencies (υ_s) of VO_4^{3-} occur at 830 cm^{-1} and 478 cm^{-1}.[43,44] The peak around 683 cm^{-1} concurs to the bending mode of vibration of Bi-O, whereas the band at 1630 cm^{-1} corresponds to adsorbing water molecules.[43,44] The IR spectrum of MBV exhibited similar peaks. The presence of peaks at around 540 cm^{-1} in the NMF spectrum assures the formation of metal-oxygen bond (Mn–O, and Ni–O), amid the (Mn and Ni) atoms and the carboxylic moiety of the 1,4 BDC ligand.[45,46, 47] The peak between 3300 and 3500 corresponds to the stretching vibration of the -OH group. The occurrence of bands at 1380 cm^{-1} and 1570 cm^{-1} is ascribed to the symmetric and asymmetric ($-COO^-$) stretching mode of vibration of the metal-ligand bond, respectively.[45,46,47] These results demonstrated that acidic -COOH deprotonated upon complexation with Mn and Ni metal ions.[47] Further, the peak appearing at 749 cm^{-1} shows out-of-plane vibration of 1,4 substituted core ring of BDC, indicating its active coordination with metal ions.[47] IR spectrum of heterostructure MBV/NMF shows similar

bands as those of MBV and NMF conforming to the absence of any impurities in nanohybrid.

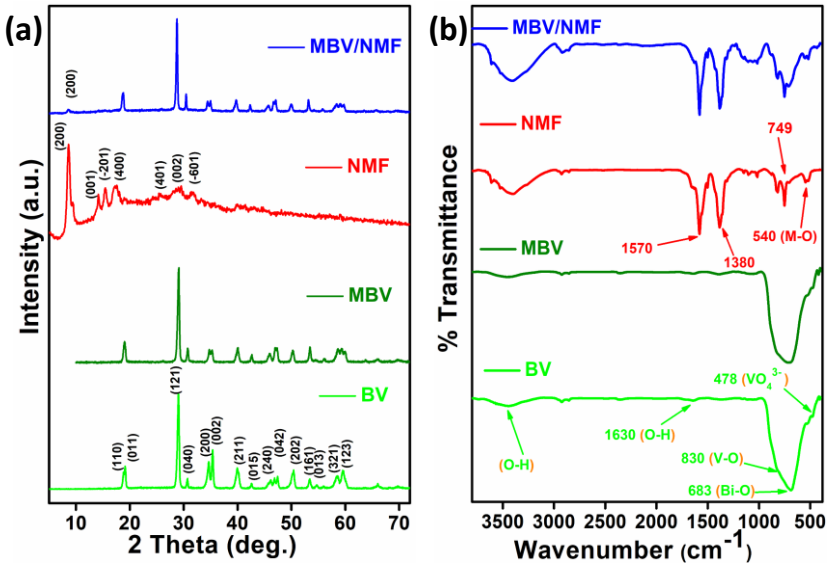

Figure 6.1. (a) XRD pattern and (b) IR spectra of BV, MBV, NMF, and MBV/NMF

For examining the morphology of BV, MBV, NMF, and nanohybrid MBV/NMF, HR-SEM photographs were taken and are demonstrated in Figures 6.2a, b, c, and d, respectively. As obvious from Figures 6.2a and b, BV and MBV reveal the nanorod morphology. The as-synthesized nanorods are irregular in size and lie between 80 nm - 700 nm. In Figure 6.2c, randomly heaped fuzzy nanosheets of NMF are manifested with a lateral size of 200-1000 nm and thickness of 15-30 nm as evaluated through image J software. Figure 6.2d reveals nanorods of MBV adorning NMF nanosheets. The EDX examination of the hybrid, Figure 6.2e, indicates the occurrence of constituent elements Mo, Bi, V, Mn, Ni, and O assuring the nanohybrid

formation. EDX spectra of $BiVO_4$, Mo-doped $BiVO_4$, and Ni/Mn-MOF are provided in Figure 6.3.

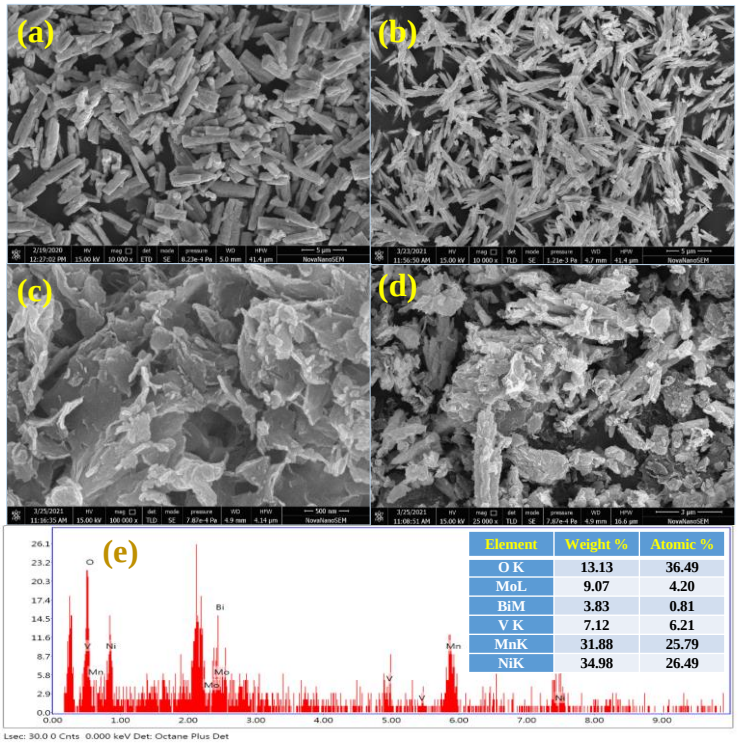

Figure 6.2. HR-SEM photographs of (a) BV, (b) MBV, (c) NMF, (d) MBV/NMF, and (e) EDX spectrum of MBV/NMF

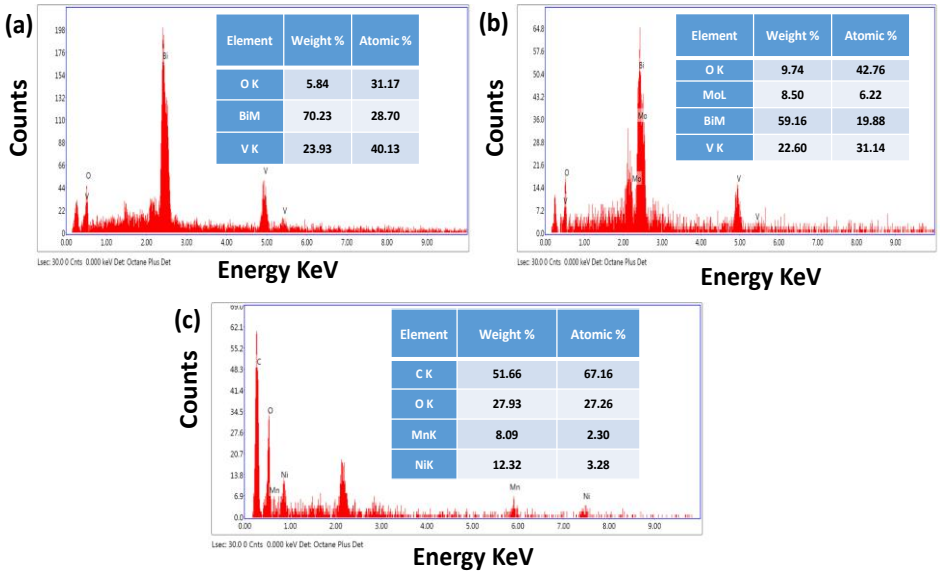

Figure 6.3. EDX spectrum of, (a) BV, (b) MBV, and (c) NMF

TEM micrographs of the synthesized additive have been taken and are portrayed in Figures 6.4a-f, for a better interpretation of the morphology. The nanorod morphologies of BV and MBV are apparent in Figures 6.4a and b. The HR-TEM picture of BV is displayed in Figure 6.4a_1. Corresponding to the (121) plane, the interplaner spacing (d-spacing) of the BV nanorod was observed to be 0.32 nm. Its selected area diffraction (SAED) pattern is displayed in the inset of Figure 6.4a_1, showing the crystalline nature. Figure 6.4c depicts the lamellar structure of NMF nanosheets. In the inset of Figure 6.4c, the semi-crystalline nature of NMF can be deduced from the SAED pattern. The anchored MBV nanorods on NMF nanosheets are visible in MBV/NMF, Figure 6.4d. According to its HR-TEM (Figure 6.4d_1), the interatomic planar distance(d_{hkl}) of the MBV nanorods of the (121) plane has increased from 0.32 to 0.34 nm in the nanohybrid. The upsurge of the inter-atomic planar distance of the (121) plane in the MBV nanorod signifies their ample interaction with the NMF nanosheets. The significant crystallinity of the nanohybrid structure can be seen from the SAED pattern, given in the inset.

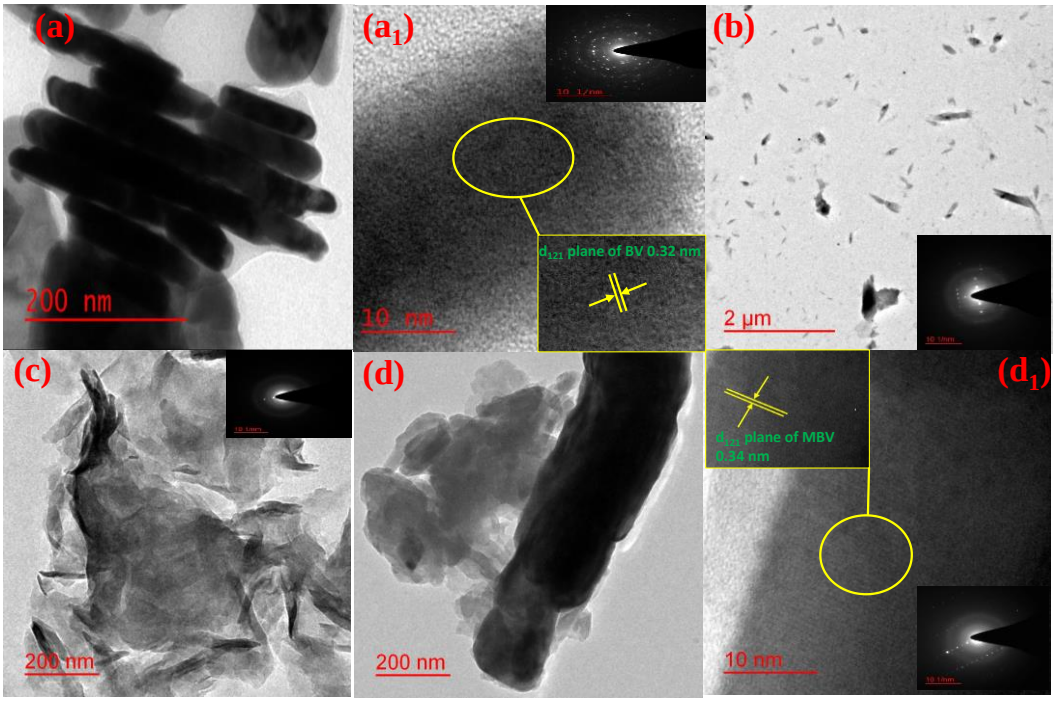

Figure 6.4. TEM photographs of (a) BV, (b) MBV, (c) NMF, (d) MBV/NMF, and HR-TEM of BV (a_1), and MBV/NMF (d_1) with SAED patterns in the insets (a_1, b, c, and d_1)

For the identification of the elemental state of the constituent elements in the hybrid MBV/NMF, X-ray Photoelectron Spectroscopy was employed. Figure 6.5 illustrates the XP spectra of Mo 3d, Bi 4f, V 2p, C 1s, O 1s, Ni 2p, and Mn 2p using XPS peak fitting software. The XP spectrum of Bi, Figure 6.5a, displays the characteristic peak of Bi^{3+} at binding energy 158.8 eV and 164.2 eV.[18,19] The peak position at 516.4 eV and 524 eV in the XP spectrum of V 2p Figure 6.5b, refers to V^{5+} metal ion.[18,19] Figure 6.5c exhibits two peaks at around binding energy 530.7 and 531.6 eV in the O 1s spectrum corresponding to the M-O bond and adsorbed water respectively.[18,19] In Figure 6.5d the XPS peaks for Mo 3d at 231.9 and 234.9 eV are observed conforming to the Mo^{+6} species in MBV.[18,19] The presence of Mo^{+6} ion validates the doping of Mo^{+6}. C 1s spectrum,

Figure 6.5e, shows peaks with binding energies 284.2 eV, 285.8 eV, and 288 eV, suggesting the C-C/C=C, C-O/C-O-C, and carboxylate groups (O=C-O), bonds of the organic BDC ligand, respectively.[42] Two major peaks in the deconvoluted Mn 2p XP spectrum correspond to $2p_{1/2}$, and $2p_{3/2}$ occurred at 653.3 eV, and 641.3 eV respectively suggesting the occurrence of Mn^{+2} possess spin-orbit coupling separation of ~12 eV (Figure 4f).[16] The peak at 646.2 eV indicates the satellite peak for Mn^{2+} ion.[16] Deconvolution of the Ni 2p XP spectrum discerns two main spin doublet corresponding to $2p_{3/2}$, and $2p_{1/2}$ at 855.5 eV, and 873.5 eV respectively having a spin-orbit coupling separation of 17 eV, showing the presence of Ni^{2+} (Figure 6.5g).[42] Moreover, in the Ni 2p XP spectra two satellite peaks at 879.5 eV, and 861.3 eV are also detected.[42]

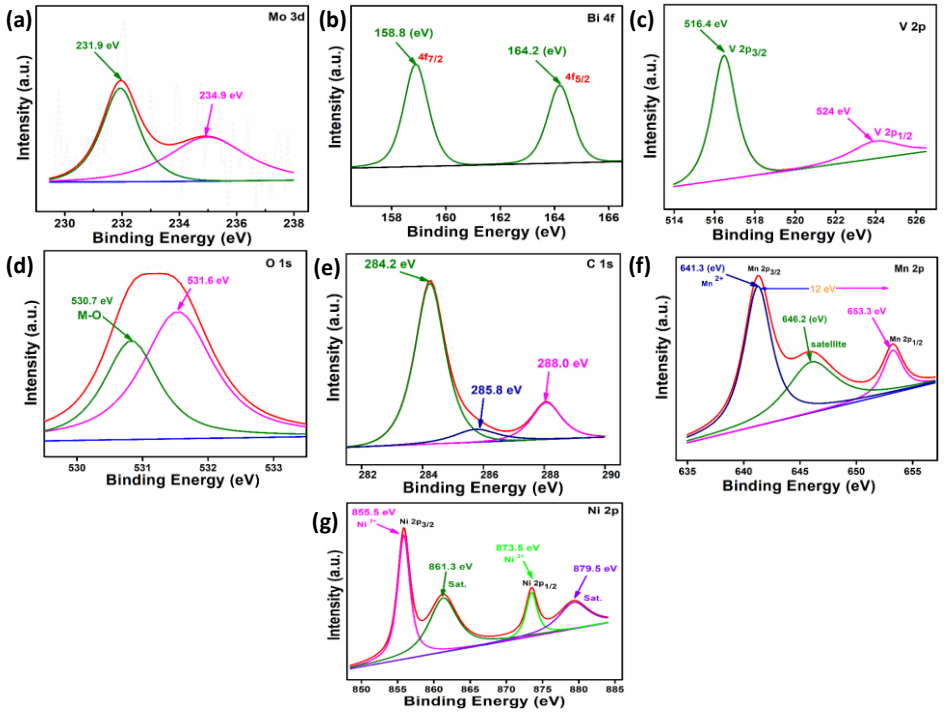

Figure 6.5. Deconvoluted XP spectra of MBV/NMF (a) Mo 3d, (b) Bi 4f, (c) V 2p, (d) O 1s, (e) C 1s, (f) Mn 2p and (g) Ni 2p

6.3.2. Tribological Characteristics

6.3.2.1. Evaluation of Dispersion Stability of Nano additives

The stability of the dispersion of the additives is extremely important for tribological outcomes. Use has been made of electronic UV/Visible spectroscopy to examine the stability of dispersion. The base lube was ultrasonically blended with the additives (at the optimal concentration) and diluted 10 times. Absorbance values were noted for diluted dispersions from 0 to 72 h at 12 h intervals. Figure 6.6a illustrates the deviation in relative absorbance with the settling time of the dispersed additive. It may be stated that the lesser the decline in relative absorbance with time, the dispersion is more stable. Thus, the nanohybrid shows the highest degree of dispersion stability, followed by NMF, MBV, and at last BV.

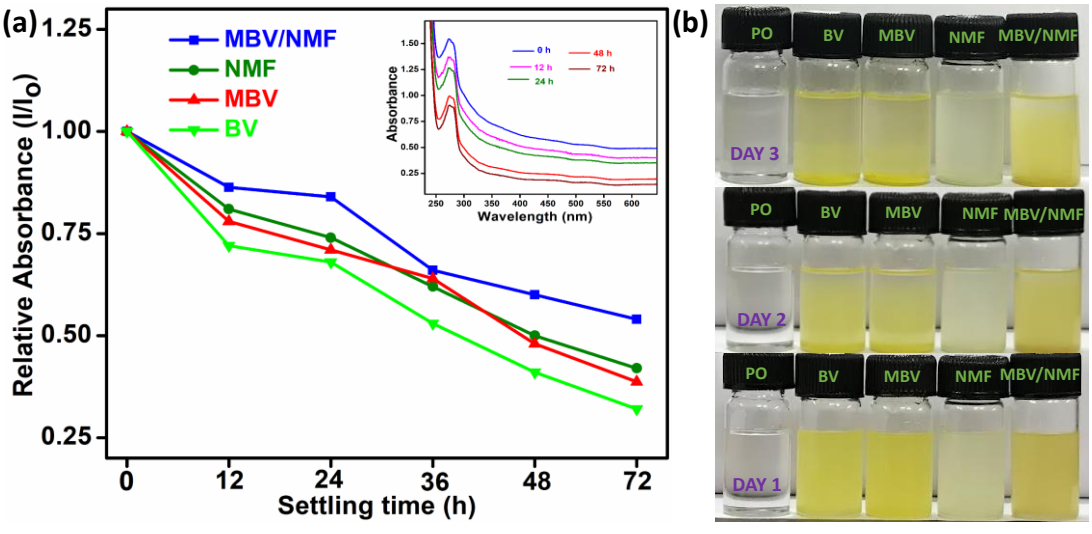

Figure 6.6. (a) Relative absorbance v/s settling time of admixtures containing BV, MBV, NMF, and MBV/NMF (b) Optical snapshots of the blends on days 1, 2, and 3

The absorbance values of the MBV/NMF at around 273 nm are displayed up to 72h at every 12h interval in the inset of Figure 6.6a. Figure 6.6b displays optical photographs of the blends of the additives on day 1, 2, and 3, showing that nanohybrid perceived maximum dispersion.

6.3.2.2. Concentration Optimization of the Additives

Concentration is a crucial term that needs to be optimized to describe the effectiveness of the additives. To do this, a standard ASTM D4172 test was performed with and without the additive in PO for various concentrations (0.00, 0.10, 0.15, 0.20, and 0.25% w/v), and evaluated their respective MWD. Figure 6.7a shows the graph of MWD vs. additive concentration. In general, the wear-diminishing character is perceived at all the examined concentrations for all the additives, however, the antiwear efficiencies differ greatly. MWD was recorded at 0.735 mm for paraffin base lube. It was found that all additives performed relatively better than PO. The MWD decreased for BV and NMF before 0.15% w/v, but thereafter it rises; however, for MBV and nanohybrid MBV/NMF, it rises after 0.1% w/v. As a result, for further tribological testing, 0.1% w/v is considered as the optimal concentration. The nanohybrid shows the supreme antiwear performance than the other nanoadditives, as shown by the variation of MWD for BV (0.570 mm), MBV (0.535 mm), NMF (0.490 mm), and MBV/NMF (0.430 mm) in descending order.

For each additive, COF optimization vs. additive concentration is shown in Figure 6.8, with the minimal antifriction performance for BV at (0.1% w/v), MBV (0.2% w/v), NMF (0.2% w/v), and MBV/NMF (0.1% w/v). In Figure 6.7b, the variation of the coefficient of friction (COF) with time is shown at the optimal concentration of 0.1% w/v. Due to

the absence of tribofilm, COF is usually substantially higher in each case in the beginning. The COF becomes stable as the running period progresses because of the in-situ tribofilm formation. The graph demonstrates how COF behaves irregularly in the absence of additives, but it is almost constant when additives are present. The evenness of the graph is associated with the nature of tribofilm. Thus, in the case of MBV/NMF the tribofilm generated is quite uniform, adherent, and stable.

6.3.2.3. Anti-friction and Antiwear Properties

To evaluate the antiwear properties of plain PO and its blends with various nanoadditives, the ASTM D4172 test was performed. The trial's outcomes are depicted in the bar diagram, Figure 6.7c, where both MWD and COF have been concurrently depicted. From the graph, it is obvious that the MWD value for base oil PO, which was 0.735 mm, has decreased in every case, demonstrating a % reduction; BV (22%), MBV (27%), NMF (33%), and MBV/NMF (42%). The decrease in MWD denotes antiwear efficacy. Since MWD has reduced by 5% from BV to MBV, Mo-doping in $BiVO_4$ has enhanced the activity. Compared to MBV, NMF, and BV, the nanocomposite is more efficacious. The % reduction in average COF value of base lube, BV (20%), MBV (25%), NMF (33%), and MBV/NMF(60%) follows a similar trend as that of MWD.

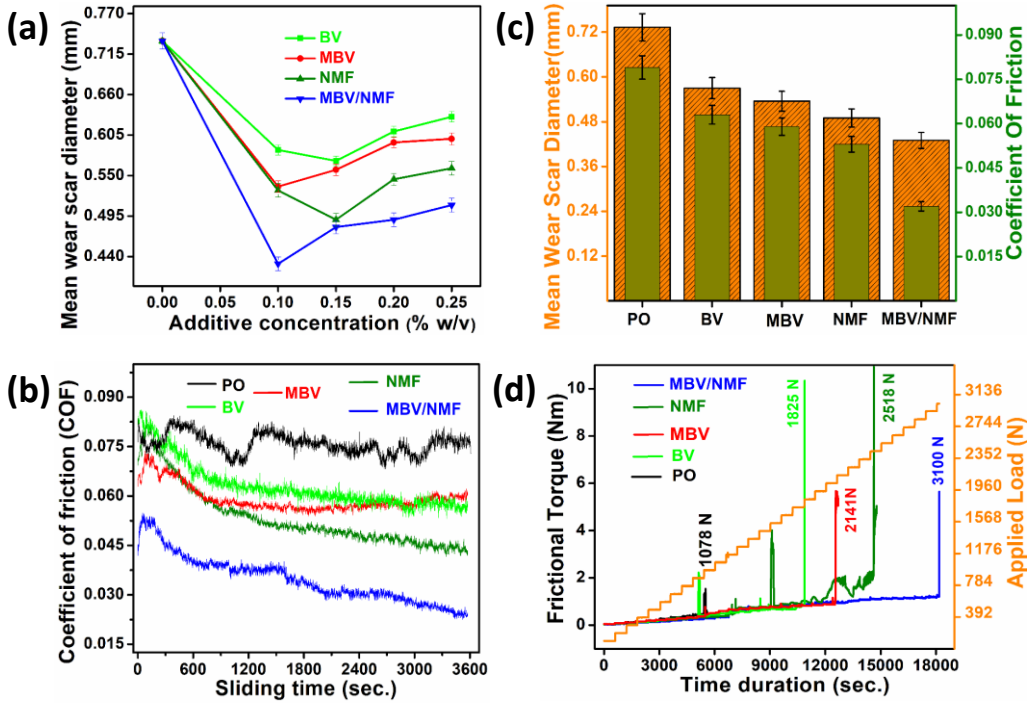

Figure 6.7. (a) MWD vs additive concentration, (b) COF vs sliding time, (c) MWD and COF in the pattern of bar diagram, and (d) Frictional torque against time and load

6.3.2.4. Load-bearing Capacity

At the optimized concentration, The ASTM D5183 standard test norms were initially carried out to complete the running-in period followed by a sequential accession of 98 N load every ten min till the seizure load is achieved due to an abrupt increase in frictional force, Figure 6.7d. At the seizure load the tribofilm ruptures, the tribosurfaces are seized and the lubricant becomes ineffective. The increase in the load-bearing ability of the PO with its admixtures inferred according to seizure load, plain PO(1078N), BV (1825 N), MBV (2141 N), NMF (2518 N), and MBV/NMF(3100 N). Thus, the exceptional load-carrying ability is perceived for the MBV/NMF. The heterogeneity of the hybrid MBV/NMF indeed supports exemplary load-carrying capability.

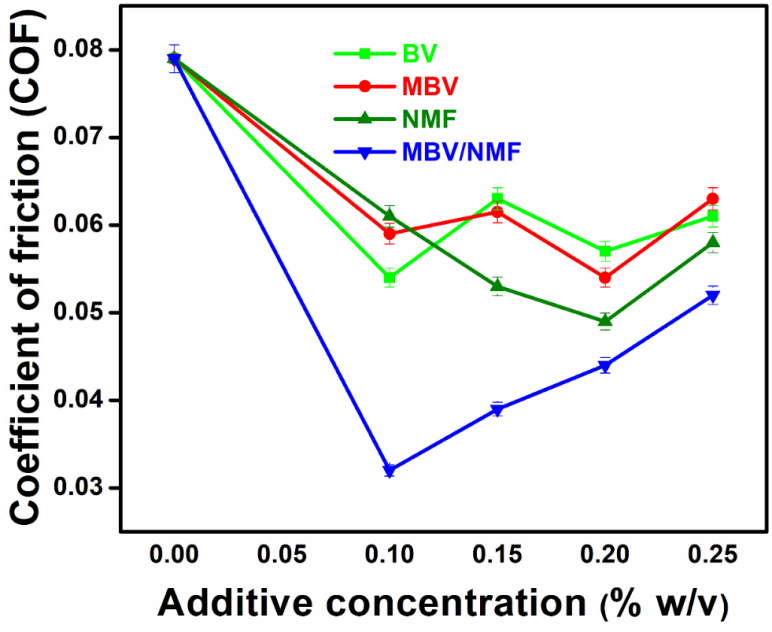

Figure 6.8. Variation of coefficient of friction (COF) vs. additive concentration

6.3.2.5. Frictional Power Loss

The evaluation of the value of frictional power loss (P) for PO in the presence and absence of the additives was carried out by utilizing equation (6.1).

$$P = 221 \times \mu \text{ (W)} \quad (6.1)$$

Where, μ = coefficient of friction

$$1 \text{ kWh} = 3.6 \text{ MJ} \quad (6.2)$$

As depicted in Table 6.1, Supreme power dissipation (0.0628 MJ) was observed in the case of base lube without any additives. For its admixtures with various additives, power consumption is significantly reduced; 0.0501 MJ for BV, 0.0472 MJ for MBV, 0.0421 MJ for NMF, and 0.0254 MJ for the hybrid. Consequently, the hybrid offers maximum energy savings.

Table 6.1. Frictional power loss value for various admixtures at optimal concentration 0.1 % (w/v)

	Additives	Power consumption (MJ)	Reduction in Power consumption	% Reduction in Power consumption
1.	PO	0.0628	_____	_____
2.	BV	0.0501	0.0127	20.22
3.	MBV	0.0472	0.0156	24.84
4.	NMF	0.0421	0.0207	32.96
5.	MBV/NMF	0.0254	0.0374	59.55

6.3.3. Morphological Attributes of Wear Track

The surface characterization performed by SEM and AFM helped to discern the morphology of the wear track surfaces after the antiwear test ASTM D4172. Figure 6.9 depicts SEM micrograph of the wear track surfaces lubricated with PO in the absence and presence of nanoadditives (0.1% w/v) The SEM micrograph of plain PO shows an uneven surface with awful scratches, however, the blended additives have assuredly improved the surface. The comparative increase in the surface evenness matches with the decrease in MWD values shown in the inset of the corresponding photograph. As expected, a notably upgraded surface is perceived in the case of MBV/NMF. The EDX investigation of the wear track is shown in Figure 6.9f, confirming the presence of all integral elements, indicating the strongly adsorbed additive on the worn surfaces. The

wear pathway EDX spectra lubricated with BV, MBV, and NMF are supplied in Figure 6.10.

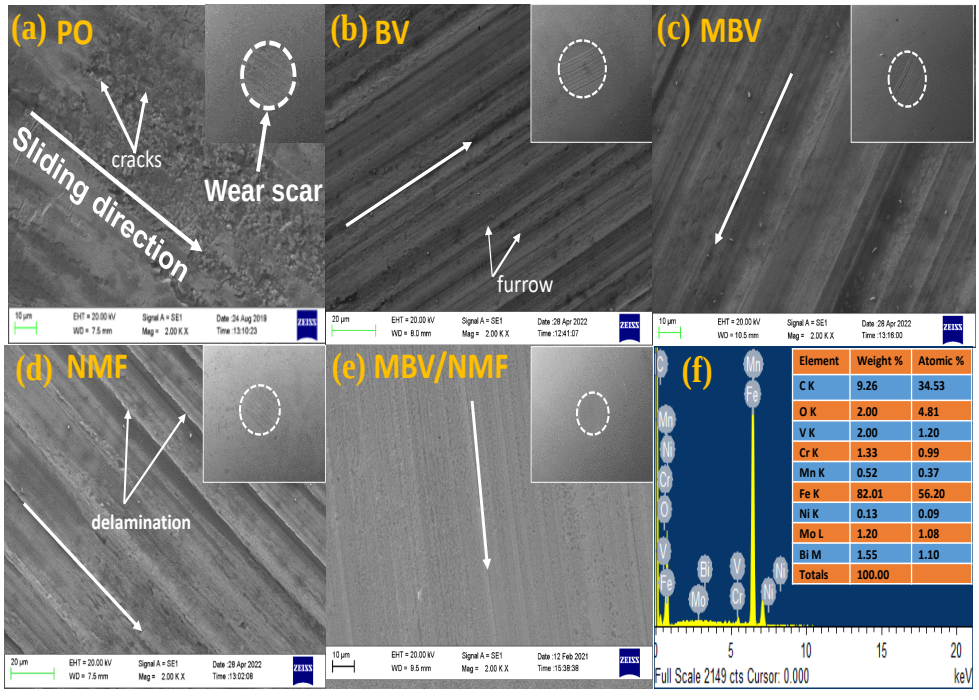

Figure 6.9. (a)-(e) SEM optical photographs of the wear track surfaces of different admixtures at 2.0 K X amplification, wear scar surfaces in the inset at 100 K X (f) EDX spectrum of wear track surfaces lubricated with MBV/NMF

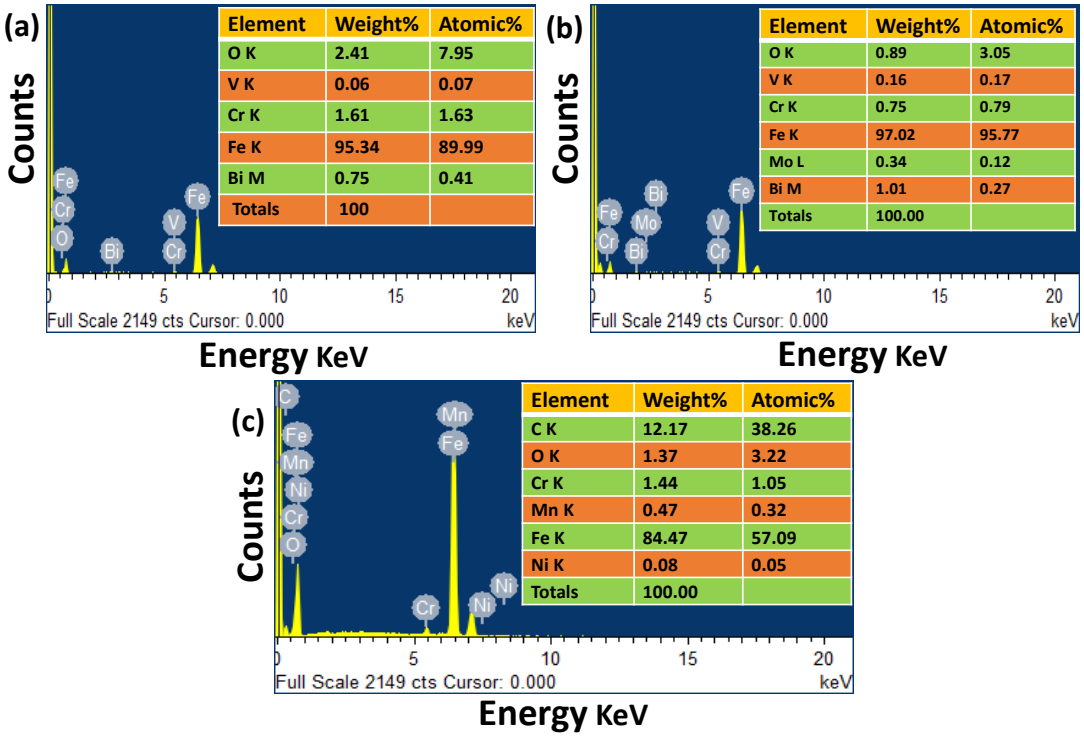

Figure 6.10. EDX spectrum of wear track of steel surface lubricated with (a) BV, (b) MBV, and (c) NMF.

After conducting the ASTM D4172 test, the roughness of the wear track surfaces was evaluated through contact mode AFM for base lube and its blends with investigated additives. The 2D/3D AFM snapshots of the surfaces of the wear track are displayed in Figure 6.11 with area roughness (Sq) and line roughness (Rq), values. The Sq and Rq values significantly decrease on moving from PO towards blended additives; BV, MBV, NMF, and MBV/NMF. Consequently, SEM together with AFM results corroborates the highest tribological efficiency of the composite MBV/NMF. Additional roughness variables like Sa, Sy, Sp, Sm, Sv, Rm, Ra, Rp, Ry, and Rv have been provided in Table 6.2.

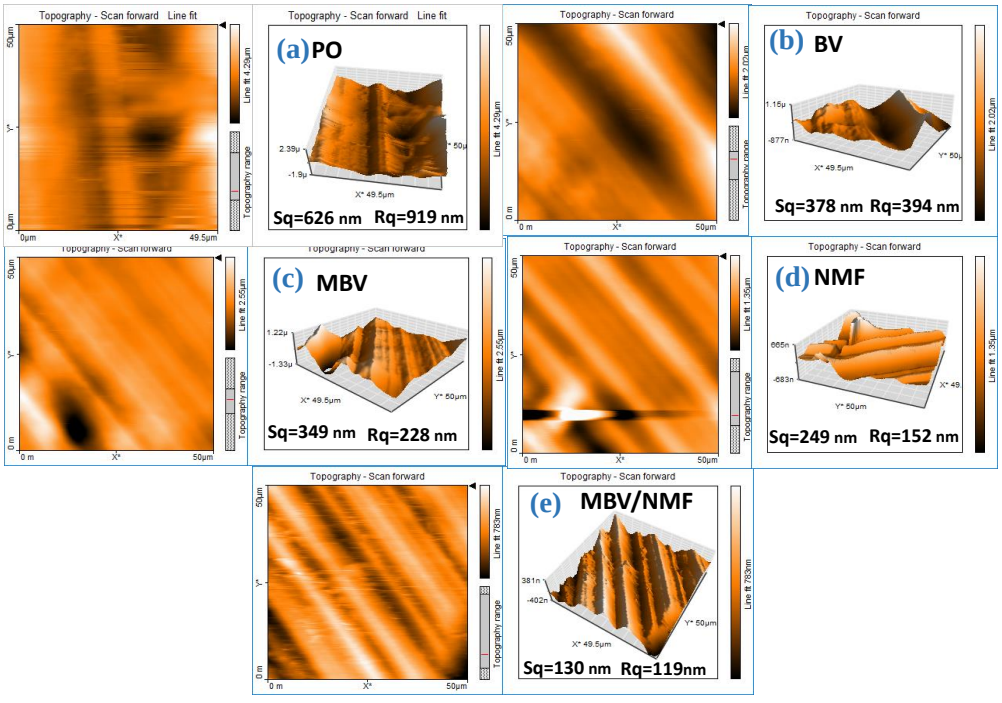

Figure 6.11. *2D* and *3D* AFM snapshots of the wear track in the presence of PO and its blends at the optimal concentration(0.1% w/v) (a) PO, (b) BV, (c) MBV (d) NMF, and (e) MBV/NMF.

Table 6.2. Surface roughness parameters obtained from the digital processing software of AFM (Nanosurf-basic Scan-2) for different additives after the antiwear test

Surface roughness parameter	Sq (nm)	Rq (nm)	Sa (nm)	Ra (nm)	Sy (nm)	Ry (nm)	Sp (nm)	Rp (nm)	Sv (nm)	Rv (nm)	Sm (pm)	Rm (pm)
PO	626	919	488	771	4363	3255	2611	2060	-1752	-1195	129	-129
BV	378	394	293	330	2117	1431	1224	721	-850	-710	194	218
MBV	344	228	230	175	2074	1175	1239	372	-1678	-802	144	146
NMF	249	152	172	132	3280	571	1845	337	-1435	-233	126	124
MBV/NMF	130	119	105	97	874	494	391	240	-482	-293	115	119

Where, S = Areal roughness, and R = Linear roughness parameters

Sq = root mean square height, Rq = root mean square line

Sa = Arithmetical mean height, Ra = Arithmetic mean line

Sy = Maximum height of the surface, Ry = Maximum height of the profile

Sp = Maximum peak height, Rp = Maximum profile peak height

Sv = Maximum valley depth, Rv = Maximum profile valley depth

Sm = Mean width area, Rm = Mean width line

6.3.3.1. Investigation of Tribofilm by XPS

Following the ASTM D4172 test, the XP spectrum of the wear track surface smeared with MBV/NMF was taken to determine the elemental states of the constituent atoms present in the in situ formed tribofilm. Using peak fit software, the core level spectra of Bi 4f, Mo 3d, O 1s, V 2p, C 1s, Mn 2p, Ni 2p, and Fe 2p are demonstrated in Figure 6.12.

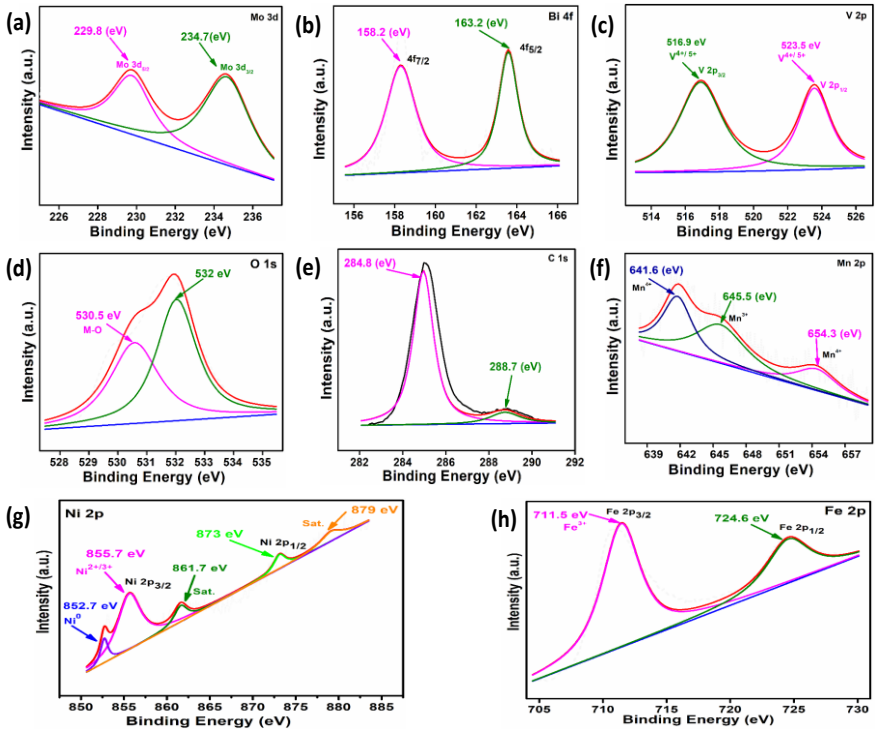

Figure 6.12. XP spectra of tribofilm formed on the worn surfaces of steel ball lubricated with MBV/NMF admixture (a) Mo 3d (b) Bi 4f (c) V 2p (d) O 1s (e) C 1s (f) Mn 2p, (g) Ni 2p, and (h) Fe 2p

The peak positions in XP spectra of Mo 3d, Bi 4f, V 2p, O 1s, C 1s, Mn 2p, and Ni 2p suggesting the formation of oxides of molybdenum (MoO_3), vanadium (VO_2,V_2O_5), nickel (NiO, Ni_2O_3), bismuth (Bi_2O_3), and manganese(MnO_2, Mn_2O_3) due to the tribochemical oxidation. [48-54, 16] Moreover, in the Fe 2p spectrum the peaks that appear at 724.2 eV (Fe $2p_{1/2}$) and, 710.5 eV (Fe $2p_{3/2}$), specify the formation of Fe_2O_3 via the oxidation of Fe of the tested steel ball.[33-39,55] Apart from this, the peak centered at about 852.7 eV in Ni 2p spectrum, corresponds to metallic Ni which can be attributed to Ni-Fe/Cr metallic alloy.[56] Thus, the metallic alloy together with several self-lubricating oxides facilitates the lubrication endorsing the tribological outcome of MBV/NMF.

6.3.4. Proposed Lubrication Mechanism

Tribological compatibility is mainly governed by the ability of an additive to adhere to the tribo-surfaces and generate load-bearing tribofilm during tribological tests. The observed efficacy of the additives essentially depends on the composition, durability, and sustainability of the tribofilm. In the presence of the composite MBV/NMF, the tribofilm formed is composed of Ni-Fe/Cr metallic alloy and various lubricious oxides of molybdenum(MoO_3), vanadium (VO_2, V_2O_5), nickel (NiO, Ni_2O_3), bismuth (Bi_2O_3), and manganese(MnO_2, Mn_2O_3), which assist in lubrication.

Certainly, a layered polymeric arrangement of NMF through weak van der Waals forces amid the proximal layers has assisted the sliding motion.[37,38] The heterogeneity of the NMF nanosheets and MBV nanorods has significantly reduced their agglomerating tendencies.[37,38,57] Nanorods have performed efficiently due to their pronounced rolling and sliding actions.[58,59] Molybdenum doping in $BiVO_4$ nanorods has improved

lubrication because of the creation of defects. It is considered that the defects promote slip systems, which affect the electronic structure and subsequently reduce shear strength.[37,39] The nanorods that lie between the nanosheets have separated the nanosheets and forbidden them from being stacked again.[23, 24, 37] Mended surfaces through the process of tribosinterization have added to the lubricious behavior.[29,37] Owing to the synergistic physical interactions amid the nanosheets and nanorods, the hybrid MBV/NMF has lived up to an outstanding tribological performance in terms of lowering wear, and friction, and boosting seizure load. A schematic diagram Figure 6.13, is provided to assist in understanding the lubrication mechanism.

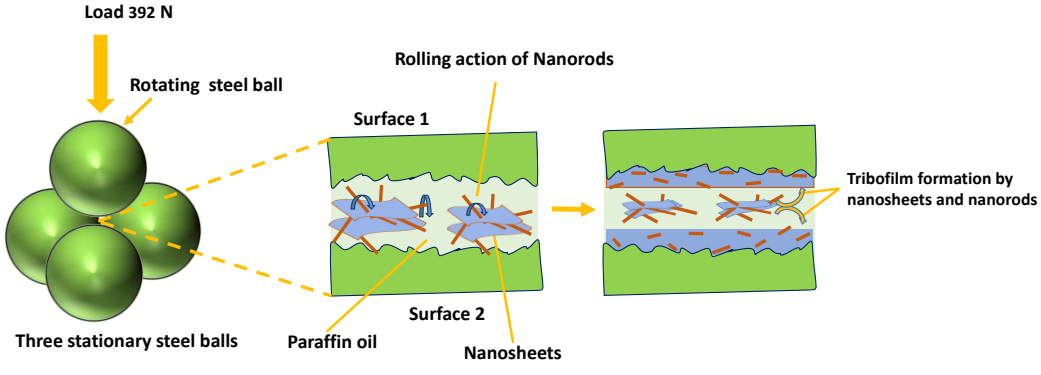

Figure 6.13. Proposed mechanism of lubrication.

6.4. Conclusions

To prevail over friction and wear losses, tribologically efficient materials are desired. Accordingly, a 2D material Ni-Mn-based bimetallic-organic framework (NMF) was synthesized ultrasonically. For the furtherance of its tribological activity, hydrothermally synthesized Mo-doped bismuth vanadate (MBV) nanorods were used to fabricate nanocomposite MBV/NMF. It was ascertained through UV/visible spectroscopy that the dispersion of the nanocomposite in base lube was stable even after 72 h. The techniques

FT-IR, XRD, HR-SEM with EDX, XPS, and TEM/HR-TEM were utilized to characterize the as-synthesized nano additives. Structural investigation discerns that physically bonded nanorods are spread over the nanosheets. The agglomeration of nanosheets and their restacking was prevented by nanorods. With the rolling and sliding actions, nanorods supported lubrication. Mending of the surface by tribosinterization facilitated these actions. Defects caused by the molybdenum doping in $BiVO_4$ have improved lubrication even further. Assessment of antifriction/antiwear activity (ASTM D4172 test) and load-bearing ability (ASTM D5183 test) on a four-ball tester manifest the highest efficiencies for MBV/NMF followed by NMF, MBV, and BV. Undoubtedly, synergistic interactions between nanorods and nanosheets have resulted in the unparalleled tribological activity of the nanocomposite. AFM and SEM studies of the wear track surface validated the observed tribological data. According to XPS studies, the tribofilm, which is made of metallic alloy Ni-Fe/Cr and several constituent lubricious metal oxides, promotes lubrication accrediting the tribological attributes of MBV/NMF.

6.5. References

[1] Wang, H.; Liu, Y. Superlubricity achieved with two-dimensional nano-additives to liquid lubricants. *Friction* **2020**, *8*, 1007-1024.

[2] Zhang, S.; Ma, T.; Erdemir, A.; Li, Q. Tribology of two-dimensional materials: From mechanisms to modulating strategies. Mater. Today **2019**, *26*, 67-86.

[3] Berman, D.; Erdemir, A.; Sumant, A.V. Approaches for achieving superlubricity in two-dimensional materials. *ACS nano*, **2018**, *12*(3), 2122-2137.

[4] Singh, B.; Indra, A. Designing Self-Supported Metal-Organic Framework Derived Catalysts for Electrochemical Water Splitting. *Chem. Asian J.* **2020**, *15*(6), 607-623.

[5] Dutta, S.; Liu, Z.; Han, H.; Indra, A.; Song, T. Electrochemical energy conversion and storage with zeolitic imidazolate framework derived materials: a perspective. *ChemElectroChem* **2018**, *5*(23), 3571-3588.

[6] Wu, H.B.; Lou, X.W. Metal-organic frameworks and their derived materials for electrochemical energy storage and conversion: Promises and challenges. *Sci. Adv.* **2017**, *3*(12), 9252.

[7] Zhao, Y.; Song, Z.; Li, X.; Sun, Q.; Cheng, N.; Lawes, S.; Sun, X. Metal-organic frameworks for energy storage and conversion. *Energy Storage Mater.* **2016** *2*, 35-62.

[8] Peng, Y.; Li, Y.; Ban, Y.; Yang, W. Two-dimensional metal–organic framework nanosheets for membrane-based gas separation. Angew. Chem. Int. Ed. **2017**, *129*(33), 9889-9893.

[9] Xiao, X.; Zou, L.; Pang, H.; Xu, Q. Synthesis of micro/nanoscaled metal–organic frameworks and their direct electrochemical applications. Chem. Soc. Rev **2020**, *49*(1), 301-331.

[10] Li, X.; Yang, X.; Xue, H.; Pang, H.; Xu, Q. Metal–organic frameworks as a platform for clean energy applications. *EnergyChem* **2020**, *2*(2), 100027.

[11] Khandelwal, G.; Maria Joseph Raj, N.P.; Kim, S.J.. Zeolitic imidazole framework: metal–organic framework subfamily members for triboelectric nanogenerators. *Adv. Funct. Mater*. **2020**, *30*(12), 1910162.

[12] Sun, W.C.; Shi, Q.; Xu, H.; Dong, J.X. Synthesis and Tribological Properties of Zeolitic Imidazolate Framework-8 Nanocrystals and Microcrystals. *Asian J. Chem.* **2015**, *27*(1).

[13] Wang, F.F.; Fan, L.; Liu, Z.; Cheng, Z.L. Surfactant-mediated preparation and tribological behaviors of few-layer ZnBDC. *Mater. Lett.* **2019**, *257*, 126757.

[14] Gao, D.Y.; Liu, Z.; Cheng, Z.L. 2D Ni-Fe MOF nanosheets reinforced poly (vinyl alcohol) hydrogels with enhanced mechanical and tribological performance. *Colloids Surf. A Physicochem. Eng. Asp.* **2021**, *610*, 125934.

[15] Zhang, G.; Xie, G.; Si, L.; Wen, S.; Guo, D. Ultralow friction self-lubricating nanocomposites with mesoporous metal–organic frameworks as smart nanocontainers for lubricants. *ACS Appl. Mater. Interfaces* **2017**, *9*(43), 38146-38152.

[16] Singh, A.K.; Yadav, A.; Indra, A.; Rastogi, R.B. Superior performance of ultrathin metal-organic framework nanosheets for antiwear and antifriction testing. *Colloids Surf. A Physicochem. Eng. Asp.* **2021**, *613*, 126100.

[17] Chen, Y.S.; Lin, L.Y.; Ma, J.S. Synthesizing molybdenum-doped bismuth vanadate nanoneedle array as photocatalyst for water oxidation using bifunctional molybdenum as dopant and structure directing agent. *Electrochim. Acta* **2020**, *329*, 135171.

[18] Mali, S.S.; Park, G.R.; Kim, H.; Kim, H.H.; Patil, J.V.; Hong, C.K. Synthesis of nanoporous Mo: $BiVO_4$ thin film photoanodes using the ultrasonic spray technique for visible-light water splitting. *Nanoscale Adv.* **2019,** *1*(2), 799-806.

[19] Qi, J.; Kong, D.; Liu, D.; Pan, L.; Chen, Y.; Zhang, X.; Zou, J.J. Bimetallic phosphide decorated Mo–$BiVO_4$ for significantly improved photoelectrochemical activity and stability. *RSC adv.* **2019**, *9*(27), 15629-15634.

[20] Singh, D.P.; Polychronopoulou, K.; Rebholz, C.; Aouadi, S.M. Room temperature synthesis and high temperature frictional study of silver vanadate nanorods. *Nanotechnology*, **2010**, *21*(32), 325601.

[21] Liu, E.; Gao, Y., Bai, Y.; Yi, G.; Wang, W.; Zeng, Z.; Jia, J. Tribological properties of self-lubricating NiAl/Mo-based composites containing $AgVO_3$ nanowires. *Mater. Charact.* **2014**, *97*, 116-124

[22] Fengzhen, L.I.U.; Xin, S.H.A.O.; Yibin, Y.I.N.; Limin, Z.H.A.O.; Zhuwei, S.H.A.O.; Xuehua, L.I.U.; Xianhua, M.E.N.G. Shape controlled synthesis and tribological properties of $CeVO_4$ nanoparticles as lubricating additive. *J. Rare Earths* **2011**, *29*(7), 688-691.

[23] Fei, J.; Luo, D.; Huang, J.; Zhang, C.; Duan, X.; Zhang, L. Growth of aligned ZnO nanorods on carbon fabric and its composite for superior mechanical and tribological performance. *Surf. Coat. Technol.* **2018**, *344*, 433-440.

[24] Luo, D.; Fei, J.; Zhang, C.; Li, H.; Zhang, L.; Huang, J. Optimization of mechanical and tribological properties of carbon fabric/resin composites via controlling ZnO nanorods morphology. *Ceram. Int.* **2018**, *44*, 15393-15401.

[25] Zhang, J.; Zhang, J. Surfactant inducing phase change of ZnO nanorods to low friction. *Tribol. Lett.* **2013,** *49*, 77-83.

[26] Lin, Z.; Jia, X.; Yang, J.; Li, Y.; Song, H. Interfacial modification and tribological properties of carbon fiber grafted by TiO_2 nanorods reinforced novel depolymerized thermosetting composites. *Compos. Part A Appl. Sci. Manuf.* **2020**, 105860-105870.

[27] Kumar, N.; Bhaumik, S.; Sen, A.; Shukla, A. P.; Pathak, S. D. One-pot synthesis and first-principles elasticity analysis of polymorphic MnO_2 nanorods for tribological assessment as friction modifiers. *RSC Adv.* **2017**, *7*, 34138-34148.

[28] Chen, L.; Zhu, D. Preparation and tribological properties of unmodified and oleic acid-modified CuS nanorods as lubricating oil additives. *Ceram. Int.* **2017**, *43*, 4246-4251.

[29] Song, H. J.; Jia, X. H.; Li, N.; Yang, X. F.; Tang, H. Synthesis of α-Fe_2O_3 nanorod/graphene oxide composites and their tribological properties. *J. Mater. Chem.* **2012**, *22*, 895-902.

[30] Liu, C.; Yan, H.; Chen, Z.; Yuan, L.; Liu, T. Enhanced tribological properties of bismaleimides filled with aligned graphene nanosheets coated with Fe_3O_4 nanorods. *J. Mater. Chem. A* **2015**, *3*, 10559-10565.

[31] Qiang, H.; Wang, T.; Qu, H.; Zhang, Y.; Li, A.; Kong, L. Tribological and rheological properties of nanorods–Al_2O_3 as additives in grease. *P. I. Mech. Eng. J-J Eng.* **2019**, *233*, 605-614.

[32] Gu, K.C.; Chen, B.S.; Wang, X.M.; Jiu, W.A.N.G.; Fang, J.H.; Jiang, W.U.; Huang, L.C.. Preparation, friction and wear properties of hydrophobic lanthanum borate nanorods in rapeseed oil. *Trans. Nonferrous Met. Soc. China* **2014**, *24*(11), 3578-3584.

[33] Verma, D. K.; Shukla, N.; Kumar, B.; Singh, A. K.; Shahu, K.; Yadav, M.; Rhee, K. Y.; Rastogi, R. B. Synergistic Tribo-Activity of Nanohybrids of Zirconia/Cerium-Doped Zirconia Nanoparticles with Nano Lamellar Reduced Graphene Oxide and Molybdenum Disulfide. *Nanomaterials* **2020**, *10*, 707-726.

[34] Verma, D. K.; Kumar, B.; Kavita.; Rastogi, R. B. Zinc oxide-and magnesium-doped zinc oxide-decorated nanocomposites of reduced graphene oxide as friction and wear modifiers. *ACS Appl. Mater. Interfaces* **2018**, *11(2)*, 2418-2430.

[35] Rastogi, R. B.; Kumar, D. Synthesis, characterization, and tribological evaluation of SDS-stabilized magnesium-doped zinc oxide ($Zn_{0.88}Mg_{0.12}O$) nanoparticles as efficient antiwear lubricant additives. *ACS Sustain. Chem. Eng*. **2016**, *4*, 3420-3428.

[36] Kalyani.; Jaiswal, V.; Rastogi, R. B.; Kumar, D. The investigation of different particle size magnesium-doped zinc oxide ($Zn_{0.92}Mg_{0.08}O$) nanoparticles on the lubrication behavior of paraffin oil. *Appl. Nanosci*. **2017**, *7*, 275-281.

[37] Singh, A. K.; Shukla, N.; Verma, D. K.; Kavita.; Kumar, B.; Rastogi, R.B. Enhancement of Triboactivity of Nanolamellar Graphitic-C_3N_4 by N-Doped ZnO Nanorods. *Ind. Eng. Chem. Res*. **2021**, *60(2)*, 864-874.

[38] Shukla, N.; Verma, D. K.; Singh, A. K.; Kumar, B., Kavita; Rastogi, R. B. Ternary Composite of Methionine-Functionalized Graphene Oxide, Lanthanum Doped Yttria Nanoparticles, and Molybdenum Disulfide Nanosheets for Thin Film Lubrication. *ACS Appl. Nano Mater.* **2020**, *3*, 8012-8026

[39] Singh, A. K.; Shukla, N.; Verma, D. K.; Kumar, B.; Mandal, K. D.; Rastogi, R.B. Reinforcement of nanoporous lanthanum-doped zinc borate by vanadium selenide nanosheets for improved tribological activity. *RSC Adv*. **2022**, *12(29)*, 18685-18696.

[40] Jo, W.K.; Natarajan, T.S. Fabrication and efficient visible light photocatalytic properties of novel zinc indium sulfide ($ZnIn_2S_4$)–graphitic carbon nitride (g-

C_3N_4)/bismuth vanadate ($BiVO_4$) nanorod-based ternary nanocomposites with enhanced charge separation via Z-scheme transfer. *J Colloid Interface Sci.* **2016**, *482*, 58-72.

[41] Kang, X.; Ma, Y.; Wang, J.; Shi, X.; Liu, B.; Ran, F.; Fabrication and properties of coral-like Ni/Mn-MOFs as electrode materials for supercapacitors. *J. Mater. Sci.: Mater. Electron.* **2021**, *32*, 13430-13439.

[42] Han, Y.; Zhou, J.; Wang, L.; Xing, L.; Xue, Z.; Jiao, Y.; Pang, Y. Redox-active nanostructure electrode of Mn/Ni bimetal organic frameworks anchoring on multi-walled carbon nanotubes for advanced supercapacitor. *J. Electroanal. Chem.* **2021**, *882*, 114993.

[43] Nagabhushana, G.P.; Nagaraju, G.; Chandrappa, G.T.; Synthesis of bismuth vanadate: its application in H_2 evolution and sunlight-driven photodegradation. *J. Mater. Chem. A* **2013**, *1*(2), 388-394.

[44] Fang, S.; Xue, S.; Wang, C.; Wang, G.; Wang, X.; Liang, Q.; Li, Z.; Xu, S. Fabrication and characterization of CdS/$BiVO_4$ nanocomposites with efficient visible light driven photocatalytic activities. *Ceram. Int.* **2016**, *42*(3), 4421-4428.

[45] Nagaraju, G.; Sekhar, S.C.; Ramulu, B.; Hussain, S.K.; Narsimulu, D.; Yu, J.S. Ternary MOF-based redox active sites enabled 3D-on-2D nanoarchitectured battery-type electrodes for high-energy-density supercapatteries. *Nano-Micro Lett.* **2021**, *13*, 1-18.

[46] Thangasamy, P.; Shanmuganathan, S.; Subramanian, V. A. NiCo-MOF nanosheet array based electrocatalyst for the oxygen evolution reaction. *Nanoscale Adv.* **2020**. *2*(5), 2073-2079.

[47] Sundriyal, S.; Mishra, S.; Deep, A. Study of manganese-1, 4-benzenedicarboxylate metal organic framework electrodes based solid state symmetrical supercapacitor. *Energy Procedia*, **2019**, *158*, 5817-5824.

[48] Tang, W.; Liu, R.; Lu, X.; Zhang, S.; Liu, S. Tribological behavior of lamellar molybdenum trioxide as a lubricant additive. *Materials*, **2018**, *11*(12), 2427.

[49] Shinde, P.V.; Ghule, B.G.; Shaikh, S.F.; Shinde, N.M.; Sangale, S.S.; Jadhav, V.V.; Yoon, S.Y.; Kim, K.H.; Mane, R.S. Microwave-assisted hierarchical bismuth oxide worm-like nanostructured films as room-temperature hydrogen gas sensors. *J. Alloys Compd.* **2019**, *802*, 244-251.

[50] Singh, A.K.; Shukla, N.; Verma, D.K.; Kumar, B.; Singh, S.; Rastogi, R.B. Polyaniline intercalated vanadium pentoxide nanosheets for the improvement of lubricity of base oil. *Colloids Surf. A Physicochem. Eng. Asp.* **2022**, *642*, 128644.

[51] Wang, L.; Liu, W.; Wang, X. The preparation and tribological investigation of Ni–P amorphous alloy nanoparticles. *Tribol. lett.* **2010**, *37*, 381-387.

[52] Li, J.; Xiong, D. Tribological behavior of graphite-containing nickel-based composite as function of temperature, load and counterface. *Wear* **2009**, *266*(1-2), 360-367.

[53] Zheng, X.; Zhang, Y.; Liu, H.; Fu, D.; Chen, J.; Wang, J.; Zhong, C.; Deng, Y.; Han, X.; Hu, W. In situ fabrication of heterostructure on nickel foam with tuned composition for enhancing water-splitting performance. *Small*, **2018**, *14*(50), 1803666.

[54] Jaffar, S.S.; Soud, W.A.; Baqer, I.A. A comparative study between two lubrication nano-additives (Bi_2O_3 & TiO_2) based on vibration response analysis. *Eng. Technol. J.* **2023**, *41*(01), 60-68.

[55] Singh, A.K.; Shukla, N.; Kumar, B.; Verma, D.K.; Maurya, J.L.; Singh, S.; Rastogi, R.B. Improvement of tribo-active behavior of g-C_3N_4 nanosheets using m-$LaVO_4$ nanoparticles. *Colloids Surf. A Physicochem. Eng. Asp.* **2023**, *663*, 131031.

[56] Zhu, Y.; Liu, T.; Li, L.; Song, S.; Ding, R. Nickel-based electrodes as catalysts for hydrogen evolution reaction in alkaline media. *Ionics*, **2018**, *24*(4), 1121-1127.

[57] Shukla, N.; Singh, A.K.; Kavita; Verma, D.K.; Kumar, B.; Maurya, J.L.; Tiwary, D.; Rastogi, R.B. Heterolamellar Bi_2Se_3/Bi_2WO_6 and Bi_2Se_3/N-Doped Bi_2WO_6 Nanosheet Composites as Potential Antifriction and Antiwear Agents. *ACS Appl. Energy Mater.* **2023**, *1*(5), 1322-1334.

[58] Gusain, R.; Khatri, O.P. Ultrasound assisted shape regulation of CuO nanorods in ionic liquids and their use as energy efficient lubricant additives. *J. Mater. Chem. A* **2013,** *1*, 5612-5619.

[59] Akbulut, M.; Belman, N.; Golan, Y; Israelachvili, J. Frictional properties of confined nanorods. *Adv. Mater.* **2006**, *18*, 2589.